

On the formation of Taylor bubbles in small tubes

Wael Salman, Asterios Gavriilidis, Panagiota Angelis*

Department of Chemical Engineering, University College London, Torrington Place, London WC1E 7JE, UK

Received 31 August 2005; received in revised form 22 May 2006; accepted 22 May 2006

Available online 3 June 2006

Abstract

The formation of Taylor bubbles and resulting bubble lengths were studied in a 1 mm ID vertical tube for air–water and air–octane systems. In the co-flow tube/nozzle arrangement two nozzle sizes were used as gas inlets. Superficial velocities varied between 0.001–0.025 m/s for the liquid and 0.002–0.04 m/s for the gas. Three different mechanisms of initial bubble formation were observed. Of the three mechanisms, mechanism 3 is periodic (with period consisting of a bubble and a liquid slug), reproducible and can be simply modelled. After initial bubble formation further modifications may occur in the formed bubble size by coalescence or pairing. Bubble pairing is encouraged by smaller nozzles and liquid flow rates, while coalescence is observed only for cases where non-Taylor bubbles form initially.

Two simple models have been proposed, the first predicts the size of the Taylor bubbles formed by mechanism 3 while the second attempts to predict the condition for bubble pairing to occur. Reasonable agreement with experimental results validates the predictions of the first model for a strong dependence of the volume of Taylor bubbles formed on the gas and liquid flow rates, a moderate dependence on nozzle diameter and a weak dependence (if at all) on the surface tension of the liquid used. Mismatch with the experimental results is caused (at least in part) by the experimental setup where there was no perfect axial alignment of the gas inlet. The experiments also suffered from problems at the outlet at low flow rates where smooth bubble disengagement could not be ensured for long Taylor bubbles. The second model for pairing predicts its occurrence for concentric tube/nozzle arrangements as a function of flow rates and channel diameters. The model over-predicted the range of liquid flow rates at which pairing was observed experimentally, but it captured the form of the boundary between different bubble volume modification mechanisms when represented on superficial velocity graphs.

© 2006 Elsevier Ltd. All rights reserved.

Keywords: Multiphase flow; Taylor flow; Taylor bubble formation mechanisms; Microchannels

1. Introduction

When surface tension forces dominate over gravity forces in a multiphase flow through a channel then the channel is described as small. This usually occurs for $Eo = g\Delta\rho d^2/\gamma < 3.37$ (Bretherton, 1961). Taylor flow is the dominant two-phase flow pattern in small channels for medium to small gas and liquid superficial velocities (Triplett et al., 1999). It consists of elongated bubbles with equivalent diameter usually many times that of the channel diameter, separated by liquid slugs. The bubbles adopt a characteristic capsular shape. Depending on the contact angle with the wall, they either completely (Serizawa et al., 2002) or nearly completely fill the channel cross section where at most a thin liquid film separates them from the channel wall

(Chen, 1986). Because of the presence of bubbles in front and at the back of the slugs, the flow field in the liquid slug is modified compared to single-phase flow and toroidal vortices extending the length of the slug are formed for capillary numbers $Ca < 0.45$ (Thulasidas et al., 1997).

As a result of the modification of the liquid flow field Taylor flow offers many advantages as compared to single-phase laminar flow (Irandoost and Andersson, 1988) in particular:

1. The separation of the bulk liquid with the bubbles significantly reduces axial mixing in the liquid (Thulasidas et al., 1999; Salman et al., 2004). The film surrounding the bubbles is the only means of communication between two successive slugs and in the majority of cases its thickness is only a fraction of a percentage of the tube diameter.

2. The recirculation within the liquid slugs improves heat and mass transfer from liquid to wall and interfacial mass transfer from gas to liquid (Berčic and Pintar, 1997).

* Corresponding author. Tel.: +44 (0) 20 7679 3832;

fax: +44 (0) 20 7383 2348.

E-mail address: p.angeli@ucl.ac.uk (P. Angelis).

With intensifying research on miniaturisation of chemical engineering unit operations, it becomes important to investigate how the benefits of Taylor flow combine with the advantages offered by operating in microchannels. The small dimensions of the microchannels, the physical properties of liquids, the range of velocities necessary for the Taylor flow regime to be present and requirements of practical applications typically limit ranges of characteristic liquid dimensionless numbers to $Ca \lesssim 10^{-3}$ and $Re \lesssim 316$. For such ranges the bubble shape and speed are functions of Ca and are not significantly influenced by Re (Aussillous and Quéré, 2000; Giavedoni and Saita, 1999).

It has been found that during Taylor flow, gas–liquid and axial mass transfer are strongly correlated to the liquid slug length (Thulasidas et al., 1999; Berčic and Pintar, 1997). In addition, pressure drop is also dependent on the number of bubbles in the channel as well as on the length of wall perimeter wetted by the liquid slugs (Kreutzer et al., 2005). It is important therefore to be able to predict bubble and slug lengths under different fluid properties, channel design and operational parameters. Although the bubble to slug length ratio can be found from the inlet gas and liquid flow rates (Thulasidas et al., 1995), their absolute values will depend on the dynamics of the two-phase contacting at the inlet. Yet despite its importance, to the best of the authors knowledge, there is no systematic investigation on Taylor bubble formation in small channels. This is surprising given the large number of studies, both experimental and theoretical, on the movement of Taylor bubbles within channels (see for example, Taylor, 1960; Bretherton, 1961; Thulasidas et al., 1995; Edvinsson and Irandoost, 1996; Giavedoni and Saita, 1997, 1999).

Existing literature on bubble formation covers larger systems/vessels and mainly small, non-Taylor bubbles (with bubble diameter smaller than the channel diameter). Bubbles are typically produced by injecting gas into a liquid through a small orifice from which they break, usually through the influence of buoyancy. Studies were originally driven by applications such as bubble columns and fermentation vessels. In early literature, bubble formation from an orifice in an open (unconfined) liquid medium under gravity was considered (Kumar and Kuloor, 1970). As a bubble is formed, the pressure within the bubble changes with the change in static pressure outside (resulting from changes of liquid head above) and the change in its surface curvature ($\Delta p = 4\gamma/d_b$ for spherical bubbles). The second term is dominant in small tubes because of the inverse dependence on diameter. If the gas is supplied at constant pressure then the gas flow rate changes with time due to changing bubble pressure. If there is a sufficiently large pressure drop, or one is introduced, between the gas reservoir and the orifice, the capillary pressure can become insignificant in comparison and the gas flow rate can be taken as constant. Two limiting cases of gas introduction can therefore be identified, constant pressure and constant flow rate (Clift et al., 1978). For intermediate cases, the volume of the gas between the reservoir and the orifice, referred to as the chamber volume, needs to be considered. Mechanistic models are usually proposed for bubble formation, based on photographic observations. For low to in-

termediate gas flow rates two different models have been suggested for bubble growth and detachment, namely single-stage and multiple-stage (for a review, see Clift et al., 1978). In the single-stage model, bubbles originating at the orifice are assumed to grow smoothly until detachment when buoyancy exceeds the attaching forces. In a multiple-stage model it is assumed that there is a basic change in the growth mechanism at one or more points in the process of formation. Typically, it is assumed that the bubbles reside on the orifice during the first stage; the second stage begins with the bubble “lift-off” and formation of a neck connecting the bubble to the orifice. At higher gas flow rates, bubble pairing has been observed at the orifice, where the forming bubble coalesces with the one formed just before. For still higher gas flow rates jetting occurs with drops forming by jet breakup.

Interesting work on non-Taylor bubble formation with flowing liquid in small tubes (small in the sense of $g\Delta\rho d^2/\gamma < 3.37$) comes from low gravity studies. Increased power demands in spacecrafts necessitate high rates of cooling and led to the study of thermally efficient two-phase flow systems under reduced gravity conditions. Bubble formation and detachment will affect in this case the distribution of the dispersed phase and the heat transfer rate. Under microgravity conditions in spacecraft, other forces usually less significant than buoyancy become important and may be used to control the bubble breakage instead. Pamperin and Rath (1995) demonstrated that the inertia of the gas injected into a liquid containing tank, may cause the bubbles to detach under reduced gravity conditions. Kamotani and coworkers studied the effect of imposing a flow around the injection orifice to cause the bubble to detach. In these studies the breakage has been simulated using a multiple-stage model for cross-flow (Kim et al., 1994; Nahra and Kamotani, 2003) and co-flow (Bhunia et al., 1998) nozzle arrangements. For higher flow rates in a co-flow arrangement, Oğuz and Zeng (1998) found that the forming bubble becomes elongated while remaining coaxial in the tube and bubbles are shed from the tip of the attached bubble, in a way similar to jetting behaviour.

Even though the studies of Bhunia et al. (1998) and Kim et al. (1994) can only be used for non-Taylor bubbles, their models are useful as they identify conditions where Taylor rather than non-Taylor bubbles are formed. Using their models, if the forming bubble diameter reaches 98% of the tube diameter without detachment, the bubble is assumed to develop into a Taylor bubble. The two models, however, cannot give any further information as to the size of the formed Taylor bubbles. Bhunia et al. (1998) studied the formation of spherical bubbles from a coaxial inlet arrangement similar to that described in this work but for larger tube diameters. A force balance on the bubble was used to identify when detaching forces overcome the attaching surface tension force anchoring the bubble to the nozzle. Subsequently the bubble moves away from the nozzle, while still attached to it by a neck. The final bubble size is achieved when the neck breaks. When the conditions were such that the bubble touches the wall before the neck breaks, Taylor bubbles were observed. For small channels surface tension forces dominate and Taylor bubbles are more likely to form.

In this work the mechanisms of Taylor bubble formation are studied experimentally in small cylindrical channels with a coaxial gas–liquid inlet arrangement, using air and either water or octane as the liquid phase. A simple model based on neck stability considerations is developed for the prediction of the Taylor bubble size for the most common of the observed mechanisms, while a second model is also suggested for predicting the conditions for bubble pairing. The model results are compared with the corresponding experimental values from this study.

2. Experimental setup

The experiments on Taylor bubble formation in microchannels were carried out in the set up shown in Fig. 1. The liquids were introduced using a 0–6 mL/min pump (milliGAT, Global FIA, Inc). The air flow rate was supplied from a gas cylinder and was regulated with a mass flow controller, MFC, (EL-FLOW F-110C, Bronkhorst). Rigid plastic tubing was used for the fluidic connections in order to reduce any effects caused by flexible tube expansion. A large pressure drop just before the gas inlet was introduced by a tube clamp to reduce the effects of pressure fluctuations during bubble formation and exit on the gas flow. Two liquids with different surface tension were chosen, *n*-octane (Fluka no. 74823, purum > 95%, GC) with properties $\gamma = 21.49 \text{ mN/m}$, $\rho = 703 \text{ kg/m}^3$ and $\mu = 10^{-3} \text{ Pa s}$ and deionised water with properties $\gamma = 72.26 \text{ mN/m}$, $\rho = 1000 \text{ kg/m}^3$ and $\mu = 8.5 \times 10^{-4} \text{ Pa s}$. Zero grade air (BOC) ($\rho = 1.19 \text{ kg/m}^3$) was used for the gas phase.

The experimental device consisted of a modified 30 cm long, 1 mm precision bore glass capillary in vertical configuration (Fig. 1). The liquid entered the capillary through a side tube joining the capillary at 90°, while the gas was introduced via a stainless steel nozzle concentric to the glass tube. Two nozzles 10 cm long were used (Hamilton, USA) with 0.64 mm OD and 0.34 mm ID and with 0.21 mm OD and 0.11 mm ID, respectively. They were held in place with a small PTFE holder and wax which also served as a sealant. The nozzles extended 4 cm above the liquid inlet to ensure developed flow of the liquid at the point where it reaches the nozzle tip and contacts the gas.

At the end of the tube a disengagement chamber was attached to help the flow of Taylor bubbles in the channel to become more regular. It was found that when the tube exit was open to the atmosphere, each time a Taylor bubble reached the exit it burst and generated a pressure fluctuation that would not only affect the movement of the other Taylor bubbles in the tube but also the bubble formation at the inlet. As the pressure fluctuation caused by the bubble burst is mostly due to the pressure difference between the inside and outside of the bubble caused by surface tension, the magnitude of these fluctuations was much larger for water because of its larger surface tension. Immersing the capillary end into a liquid reservoir reduced the pressure fluctuations but did not remove them completely as there was still a sudden change in bubble radius from that inside the tube to that in the disengagement chamber where the bubble became spherical. There was a gradual enlargement of the capillary ID at the exit, due to the chamber attachment procedure and this reduced further the sudden pressure fluctuations. For the cases where very long Taylor bubbles with volume larger than the volume of the expansion section were formed, however, the pressure fluctuations could not be eliminated.

For the observation of the Taylor bubble formation at the inlet a high-speed camera Kodak Ektapro HS 4540 was used with a 40× lens. Recording speeds of either 250 or 125 fps for the slower flow rates were found to be sufficient. The duration of the bubble formation could be found from the number of frames taken. For each experimental condition 20 or more bubbles were analysed and the times necessary to form bubbles were averaged.

3. Results

For each nozzle size and each liquid the liquid flow rate was varied from 0.06 to 1.2 mL/min and the gas flow rate was varied from 0.07 to 1.6 mL/min. These correspond to superficial velocities 0.001–0.025 m/s for the liquid and 0.002–0.04 m/s for the gas. Taylor bubble formation followed two steps (a Taylor bubble is considered “formed” when there would be no further modification to its length by pairing or coalescence

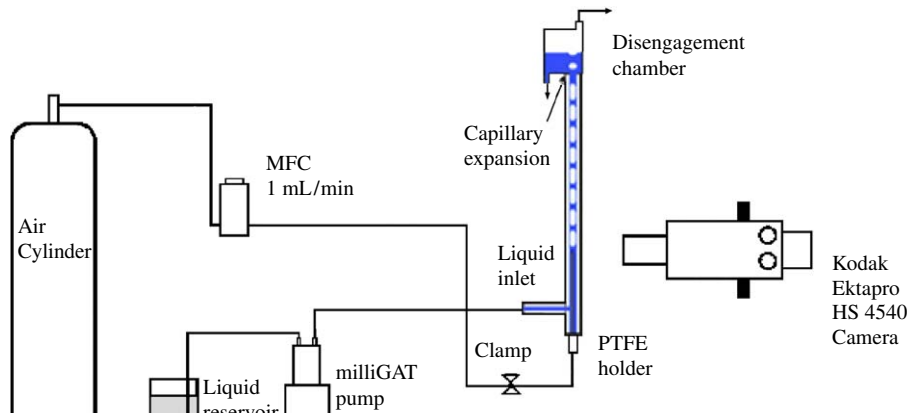


Fig. 1. Schematic view of the apparatus for the study of Taylor bubble formation in liquid.

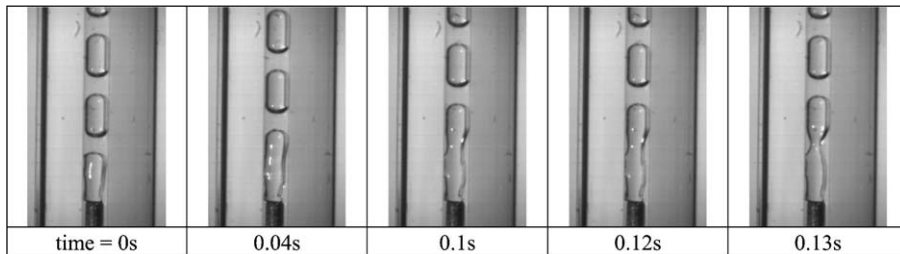


Fig. 2. Mechanism 1 for Taylor bubble formation in water for a 0.34 mm ID nozzle. Liquid superficial velocity, $U_{LS} = 0.0076 \text{ m/s}$, gas superficial velocity, $U_{GS} = 0.0190 \text{ m/s}$.

within the tube):

1. Bubble formation at the nozzle; the formed bubbles were either Taylor or non-Taylor (with their diameter less than the tube diameter).
2. Bubble size modification after its formation by pairing or coalescence inside the channel after the inlet.

It should be mentioned that having the tube and the nozzle precisely concentric could not be achieved with this apparatus. This however possibly triggered another mechanism of Taylor bubble formation which may not have occurred in more axisymmetric conditions.

3.1. Mechanisms of bubble formation

The following mechanisms were observed:

Mechanism 1 (Fig. 2) was characterised by the formation of a gas chamber ahead of the nozzle, with the gas in contact with the tube walls in one or more areas. Bubbles broke at the tip of this gas chamber. The gas in this case covered the entire top surface of the needle up to its outer diameter. The rate of bubble formation once this mechanism was initiated was stable and the bubble movement was very smooth with no pressure fluctuations associated with the bubble breakup at the inlet. However, the initiation of such a mechanism was difficult, and with changing flow rates, the size of the gas chamber changed, or even disappeared completely at high liquid flow rates.

The time periods required for the Taylor bubble formation at any fixed gas and liquid flow rates varied from extremely regular, with an error of less than $\frac{1}{250} \text{ s}$ for conditions leading to the formation of the smallest bubbles, to fluctuating for conditions leading to large bubbles (see Fig. 3). The large discrepancies in the latter case resulted from the effects of long bubbles exiting into the liquid-gas disengagement chamber. In general, for mechanism 1 time periods decreased with increasing liquid and gas flow rates with the curves becoming flatter at high flow rates. However, there were points in the trends where there seemed to be a sudden jump or fall in the period, in disagreement with the general trends. These variations arose from changes in gas chamber size and were not reproducible. This mechanism was seen for the large nozzle and water as the test fluid.

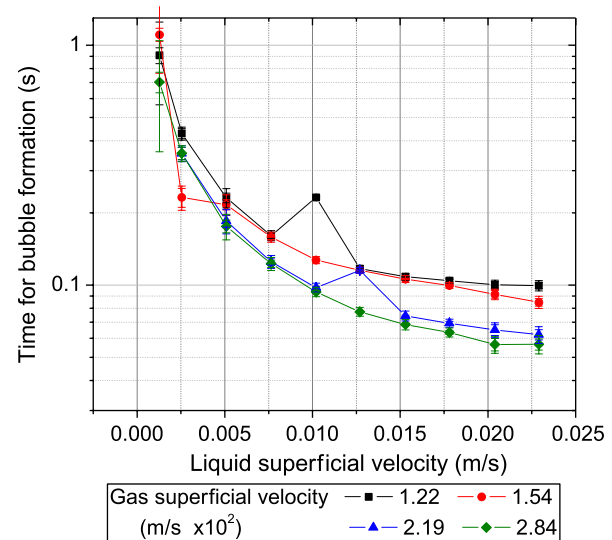


Fig. 3. Periods of bubble formation with mechanism 1 for air flow into water using a 0.34 mm ID nozzle. Error bars show the range of time variation for each condition.

Mechanism 2 (see Fig. 4) occurred at the same range of flow rates as mechanism 1 and was most dramatic at low gas flow rates. This mechanism seemed to depend on the initial conditions in the tube. If the gas was introduced into the dry tube before introducing the liquid, mechanism 1 was sometimes observed, however, the reverse always resulted in mechanism 2. In mechanism 2, at the beginning of bubble formation, the gas formed a meniscus at the nozzle tip while the pressure built up behind the meniscus. When the pressure reached a critical value the pressure inside the nozzle overcame the hydrostatic and capillary pressures and the gas broke through and very rapidly formed a bubble. At low liquid flow rates, this initial fast growth phase did not always terminate with bubble detachment from the nozzle, but the bubble would continue to grow and to form a neck at the nozzle. Eventually the bubble would detach when this neck destabilised and broke. The necking and subsequent breakage are similar qualitatively to what was usually seen in mechanism 3. Interestingly, the volume of the bubble formed did not seem to be affected by the liquid flow rate, at low to moderate liquid flow rates. Instead, an increase in the liquid flow rate simply increased the separation between the formed bubbles. As liquid flow rate was increased further, instead of

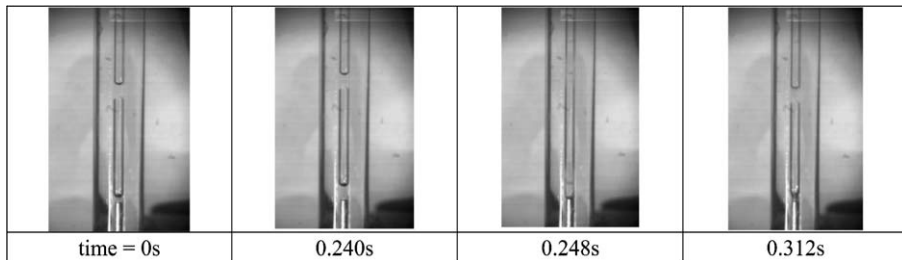


Fig. 4. Mechanism 2 for Taylor bubble formation in water for a 0.34 mm ID nozzle. There is no observed gas flow rate till 0.248 s. A rapid *burst* of gas forms most of the bubble at 0.248 s. The bubble continues to grow at a much slower rate and detaches from the nozzle at around 0.312 s. Liquid superficial velocity, $U_{LS} = 0.000632 \text{ m/s}$, gas superficial velocity, $U_{GS} = 0.00511 \text{ m/s}$.

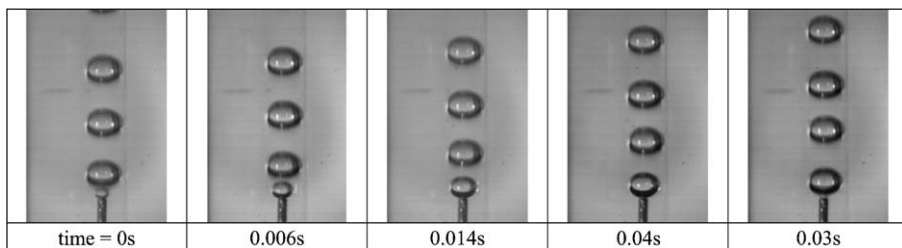


Fig. 5. Mechanism 3 of initial non-Taylor bubble formation in octane for a 0.11 mm ID nozzle. Liquid superficial velocity, $U_{LS} = 0.0178 \text{ m/s}$, gas superficial velocity, $U_{GS} = 0.0120 \text{ m/s}$.

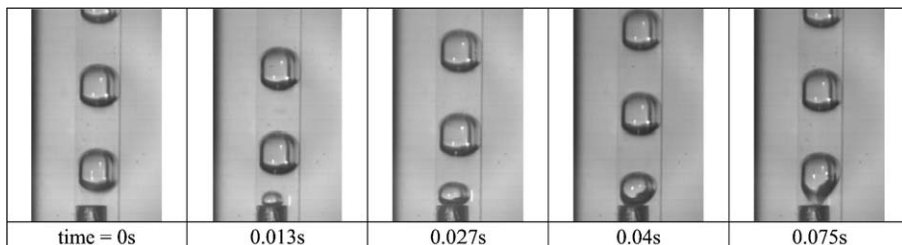


Fig. 6. Mechanism 3 of Taylor bubble formation in octane for a 0.34 mm ID nozzle. Liquid superficial velocity, $U_{LS} = 0.0178 \text{ m/s}$, gas superficial velocity, $U_{GS} = 0.0120 \text{ m/s}$.

one Taylor bubble, a number of shorter Taylor bubbles formed in the abrupt gas burst with total volume approximately the same as the initial single bubble at lower liquid flow rates. The number of these bubbles increased with increasing liquid flow rate.

Generally, mechanism 2 generated much larger bubbles for the same gas and liquid flow rates compared to mechanism 1. The movement of bubbles appeared to pulsate every time a bubble formed while the bubble volume depended mainly on the volume of gas pressurised upstream of the nozzle tip. No periods of bubble formation were collected for this mechanism.

Mechanism 3, as seen in Figs. 5–7, is similar to the non-Taylor bubble formation mechanism described in the literature (Bhunia et al., 1998). During the first stage the bubble resided on the nozzle while in the second stage the bubble “lifted-off” and a neck formed at the nozzle. When the detachment forces became larger than the attaching surface tension forces at the inlet before the forming bubble reached the channel wall, necking and breakage occurred and spherical non-Taylor bubbles

were formed (Fig. 5). The occurrence of non-Taylor bubbles is favoured by small nozzle to channel diameter ratios and weaker surface tension forces. For large nozzle to diameter ratios (compare Figs. 5 and 6) or strong surface tension forces (compare Figs. 5 and 7), the attaching forces stabilised the bubble long enough for it to grow and become a Taylor bubble. Liquid then built up behind the bubble and the shape of the back of the bubble was modified to resemble a neck. Subsequently the neck broke and the bubble was detached.

Similar to mechanism 1, the time periods necessary for Taylor bubble formation were either very regular, with an error of less than $\frac{1}{250} \text{ s}$, when small bubbles were formed, or very irregular when large bubbles were formed, caused by the pressure fluctuations as the bubbles entered into the liquid–gas disengagement chamber (Figs. 8 and 9). Results from octane and 0.11 mm ID nozzle are not reported because the bubbles formed were either small, non-Taylor or their sizes changed further in the tube after detachment due to pairing and/or coalescence (Fig. 21).

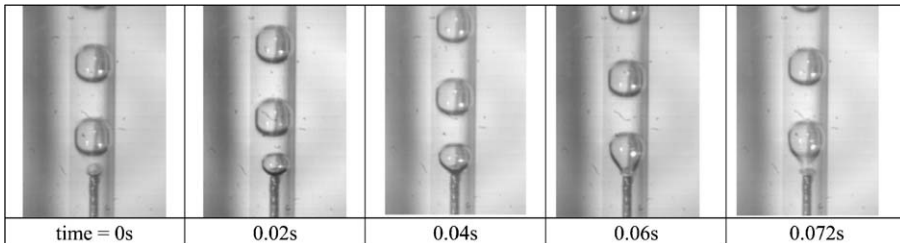


Fig. 7. Mechanism 3 of Taylor bubble formation in water for a 0.11 mm ID nozzle. Liquid superficial velocity, $U_{LS} = 0.0178 \text{ m/s}$, gas superficial velocity, $U_{GS} = 0.0120 \text{ m/s}$.

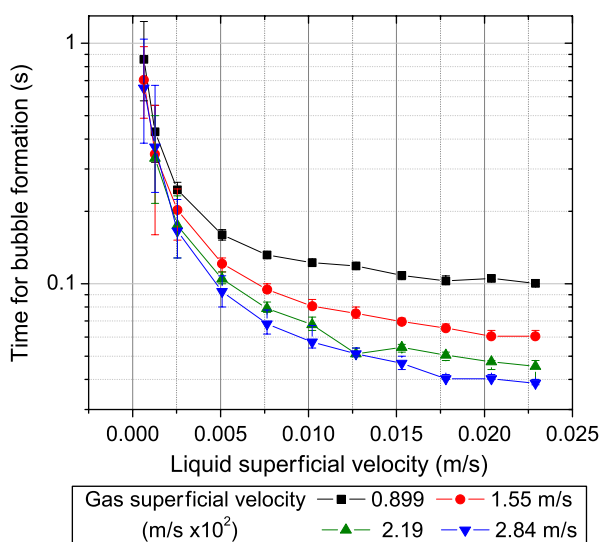


Fig. 8. Periods of bubble formation with mechanism 3 for air flow into water using a 0.11 mm ID nozzle. Error bars show the range of time variation for each condition.

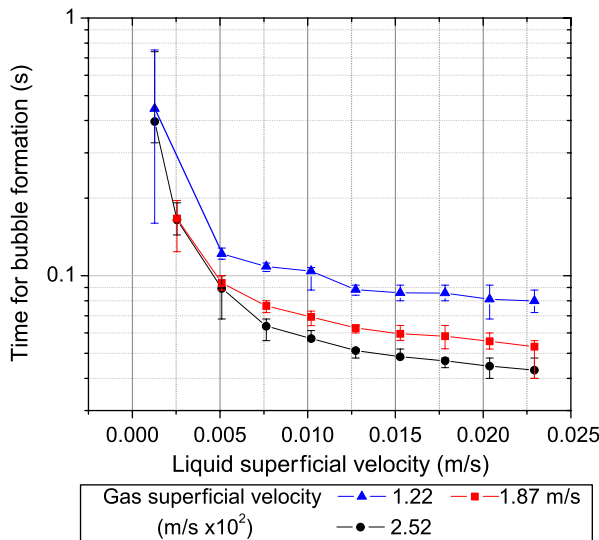


Fig. 9. Periods of bubble formation with mechanism 3 for air flow into octane using a 0.34 mm ID nozzle. Error bars show the range of time variation for each condition.

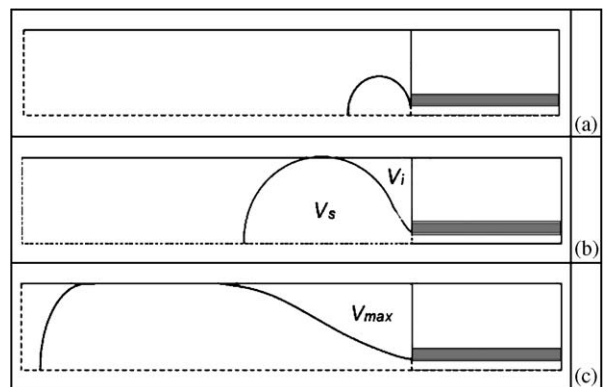


Fig. 10. The different stages in the Taylor bubble formation by mechanism 3: (a) formation of a “small” spherical bubble; (b) the spherical bubble touches the wall and becomes a Taylor bubble; (c) the point at which the neck behind the Taylor bubble becomes unstable, leading to bubble detachment from the nozzle.

The measured times for bubble formation with mechanism 3 showed regular trends of decreasing periods with increasing liquid and gas flow rates.

The inlet misalignment would not have affected mechanism 2 (where the bubble volume depends on the volume of air compressed in the nozzle behind the meniscus) or 3 where the formed neck does not touch the wall. With mechanism 1 the misalignment may have affected the range of flowrates where this mechanism appeared. However, any condition which breaks the symmetry in the introduction of the two fluids at the inlet would have caused it. Apart from the misalignment (which in microchannels can also result from manufacturing tolerances) other phenomena, such as gravity in not perfectly vertical tubes and non-symmetries in the moving three-phase contact line during the liquid introduction, would also initiate this mechanism.

3.2. Model for bubble formation by mechanism 3

3.2.1. Stages of bubble formation

The steps by which a Taylor bubble is formed by mechanism 3 are illustrated in Fig. 10. A near spherical bubble grows from the tip of the nozzle to fill the entire channel cross section without necking (Figs. 10(a) and (b)). When it touches the wall either the continuity of the bubble interface is broken to form two contact lines at the wall or the continuity of the liquid

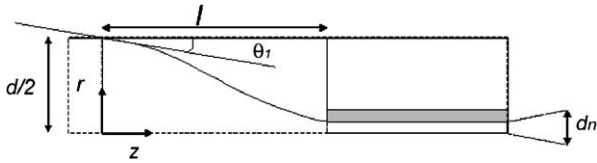


Fig. 11. A snapshot in the formation of a Taylor bubble. At the walls θ_1 is the real or apparent contact angle.

phase is preserved and a thin liquid film is formed separating the bubble from the wall. In the first case the contact angles are real, in the second they are apparent. Apparent contact angles depend on the local hydrodynamics of the flow near the wall (Chebbi, 2003). In both cases, once the bubble reaches the wall, all subsequent liquid flow will accumulate behind it (Fig. 10(c)). This is obvious when the bubble touches the wall, but would also be valid when a film forms between the bubble and the wall as the liquid flow in the film is negligibly small for the cases encountered here (e.g. see Figs. 6 and 7).

For constant gas and liquid flow rates two time parameters need to be identified whose sum adds up to the total time of bubble formation; the time necessary for the approximately spherical bubble to reach the wall, t_s , and the time between the bubble reaching the wall and detaching from the nozzle, t_t . t_s is easily calculated from Eq. (1) if bubbles are assumed spherical. This is a good approximation when compared to the experimental observations (Figs. 5–7). Higher flow rates may result in significant deviations from this assumption due to forces other than surface tension becoming important (Bhunia et al., 1998)

$$t_s = \frac{V_s}{Q_g} = \frac{\pi d^3}{6 Q_g} \quad (1)$$

t_t can be found from Eq. (2) where V_{\max} is the maximum volume of liquid behind the Taylor bubble (attained at the point of detachment) and V_i is the initial liquid volume when the bubble touches the wall (see Fig. 10(b)). V_{\max} is related to the stability of the interfacial profile at the back of the forming bubble and needs to be determined

$$t_t = \frac{V_{\max} - V_i}{Q_l} = \frac{V_{\max} - \pi d^3/24}{Q_l}. \quad (2)$$

3.2.2. Profile and stability of the meniscus at the back of the forming Taylor bubble

A snapshot of the bubble formation by mechanism 3 is given in Fig. 11. The Capillary number is $10^{-4} < Ca < 10^{-3}$, the liquid Reynolds number calculated using the average velocity in between the nozzle and tube is $2 < Re < 130$, and the Weber number, $We_l = CaRe$ is $2 \times 10^{-4} < We_l < 0.2$. These show the dominance of surface tension forces followed by inertia then viscous forces for the liquid. Neglecting both viscous and inertial forces would simplify the problem to a quasi-static system.

Based on the above, a simple model is used with the following assumptions:

- (1) The liquid flow rate is small such that its velocity does not contribute to the pressure on the meniscus (quasi-static system).
- (2) The gas is assumed to be inviscid and incompressible.
- (3) The radial pressure gradients in the gas are negligible. This can be justified from the fact that newly formed surfaces of the bubble are shear free and dimensions are small.
- (4) The real or apparent contact angle remains constant.
- (5) The bubble forming eventually becomes a Taylor bubble (This can be tested using the force balance method of Bhunia et al., 1998 if ‘lift-off’ does not occur before the bubble touches the wall).

The average gas velocity changes with changing cross section according to the continuity equation

$$u_g = u_{g0} \frac{d_n^2}{4r^2}, \quad (3)$$

where u_{g0} is the known velocity of the gas through the nozzle.

Along a streamline that follows the interface profile of the neck, the pressure p_g in the gas phase varies according to the Bernoulli equation

$$p_g = p_{g0} + \frac{1}{2} \rho_g u_{g0}^2 \left(1 - \frac{d_n^4}{16r^4} \right). \quad (4)$$

To obtain the interface profile at the back of the bubble the Young–Laplace equation is used (Hernandez-Baltazar and Gracia-Fadrique, 2005):

$$\begin{aligned} p_g - p_l &= p_{g0} + \frac{1}{2} \rho_g u_{g0}^2 \left(1 - \frac{d_n^4}{16r^4} \right) - p_l \\ &= \gamma \left[\frac{1}{r[1 + (dr/dz)^2]^{1/2}} - \frac{d^2 r / dz^2}{[1 + (dr/dz)^2]^{3/2}} \right]. \end{aligned} \quad (5)$$

This can be non-dimensionalised using d as characteristic length and γ/d as characteristic pressure as follows (“–” denotes dimensionless parameter):

$$\begin{aligned} \bar{p}_{g0} + \frac{We_g}{2} \left(1 - \frac{\bar{d}_n^4}{16\bar{r}^4} \right) - \bar{p}_l \\ = \left[\frac{1}{\bar{r}[1 + (\bar{d}r/\bar{d}\bar{z})^2]^{1/2}} - \frac{d^2 \bar{r} / d\bar{z}^2}{[1 + (\bar{d}r/\bar{d}\bar{z})^2]^{3/2}} \right]. \end{aligned} \quad (6)$$

Parameterisation of Eq. (6) using the interface arc length \bar{S} and angle α of the interface with the horizontal gives

$$\frac{d\bar{r}}{d\bar{S}} = \sin \alpha, \quad (7)$$

$$\frac{d\bar{z}}{d\bar{S}} = \cos \alpha, \quad (8)$$

$$-\frac{d\alpha}{d\bar{S}} = \Delta \bar{p} + \frac{We_g}{2} \left(1 - \frac{\bar{d}_n^4}{16\bar{r}^4} \right) - \frac{\cos \alpha}{\bar{r}}. \quad (9)$$

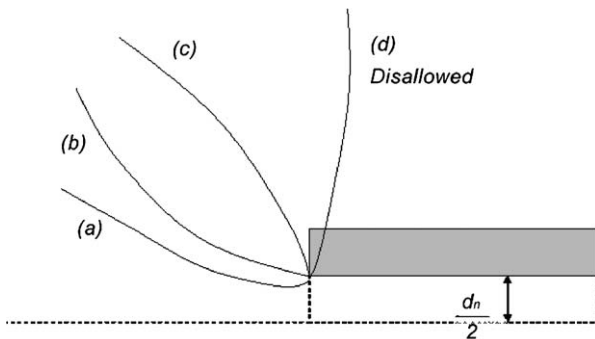


Fig. 12. Schematic of allowable angles when investigating the range of allowable interface profiles. Profile (a) where the interface dips below the nozzle radius before rising (b) with upward concavity (c) with downward concavity. Arrangement (d) shows an angle and interface which are not physically possible.

The dimensionless numbers arising from the Young–Laplace equation and the boundary conditions are:

$$\text{Gas Weber number } We_g = \rho_g u_{g0}^2 d / \gamma.$$

$$\text{Ratio of diameters } \bar{d}_n = d_n / d.$$

$$\text{Pressure difference } \Delta \bar{P} = \bar{p}_{g0} - \bar{p}_l = (d/\gamma)(p_{g0} - p_l).$$

To solve the set of Eqs. (7)–(9) two procedures can be followed based on the known end values ($r = d_n/2$ at the nozzle and $r = d/2$ at the point where the interface touches the wall) and the real/apparent contact angle at the wall. The solution can start from the nozzle by guessing a contact angle at the nozzle tip (a controlled variable) then calculating from the solution the contact angle at the wall and iteratively adjusting the guessed angle until the real/apparent contact angle at the wall is obtained. Alternatively, the solution can start at the wall with the given wall contact angle and proceed to calculate the interface profile until the nozzle radius is reached. The second method was chosen because of its convenience.

The dimensionless initial conditions are

$$\bar{r}(0) = \frac{1}{2}, \quad (10)$$

$$\bar{z}(0) = 0, \quad (11)$$

$$\alpha(0) = -\theta_1. \quad (12)$$

The set of Eqs. (7)–(9) was solved using a 5–6 order Runge–Kutta method (Mathematica 5.1, Wolfram Research Inc.) for a given $\Delta \bar{p}$, We_g and θ_1 and a sufficiently long interface arc length. The points at which the $\bar{r}(\bar{S}) = \bar{d}_n/2$ such that the apparent angle at the nozzle tip, α , is always within a range of allowable apparent angles (Fig. 12), would be valid solutions. The only profiles disallowed are those which cut the nozzle wall (profile (d)). Profile (a) differs from (b) in that it has a minimum value smaller than $\bar{d}_n/2$. Although this profile is allowed it was not experimentally observed. The arc length at that point is obtained from the numerical solution ($\bar{S} = \bar{\lambda}$) and the distance along the wall from the nozzle is $\bar{z}(\bar{\lambda}) = \bar{l}$ (Fig. 11). If $\bar{r}(\bar{S}) \neq \bar{d}_n/2$ at any value of \bar{S} , or the angle at the nozzle exceeds the physically possible angles, then for the given set of parameters, the

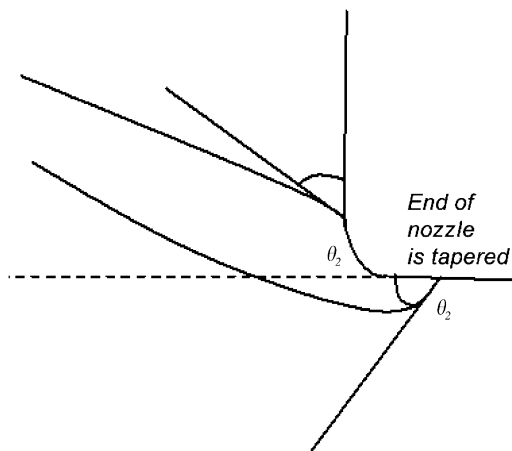


Fig. 13. For a smooth tapered nozzle, only apparent contact angles between $\theta_2 - 90^\circ < \alpha < \theta_2$ should be observed.

Table 1
Parameter values for the cases where mechanism 3 was observed

	Water	Octane
\bar{d}_n	0.11	0.34
θ_1	0°	0°
We_g	$9.09 \times 10^{-3} - 1.13 \times 10^{-1}$	$3.35 \times 10^{-4} - 4.15 \times 10^{-3}$

problem was regarded as having no solution. It is assumed that by moving from a set of parameters which give a valid solution, or solutions, to those with no solution, some instability occurs and the bubble detaches. The point at which this change took place was found for given We_g and θ_1 by trying different $\Delta \bar{p}$ values until two were found which bracket the instability point, then iteratively shrinking the bracket to that point. It should be noted that in reality $\alpha(\bar{\lambda})$ at the nozzle would be dependent on the value of the real contact angle with the material and the local surface geometry of the nozzle tip. As an example, if the nozzle tip is smooth and tapered and the receding contact angle is θ_2 , the values of $\alpha(\bar{\lambda})$ would be limited to a range between $\theta_2 - 90^\circ < \alpha(\bar{\lambda}) < \theta_2$ (see Fig. 13). Since the nozzle tip geometry is usually not known the criterion of Fig. 13 is not used in the simulations.

For a given profile, the volume of liquid behind the bubble up to the nozzle tip is given by

$$\bar{V}_l = \int_{\bar{z}=0}^{\bar{z}=\bar{l}} \pi \left(\frac{1}{4} - \bar{r}^2 \right) d\bar{z} = \int_{\bar{S}=0}^{\bar{S}=\bar{l}} \pi \left(\frac{1}{4} - \bar{r}^2 \right) \cos \alpha d\bar{S}. \quad (13)$$

The maximum value of \bar{V}_l is \bar{V}_{\max} found as $\Delta \bar{p}$ is varied. The time of bubble formation can then be easily calculated from the sum of times of Eqs. (1) and (2).

3.3. Comparison between model predictions and experimental results

The range of the parameters in the two sets of experimental data where mechanism 3 appeared is given in Table 1. It is

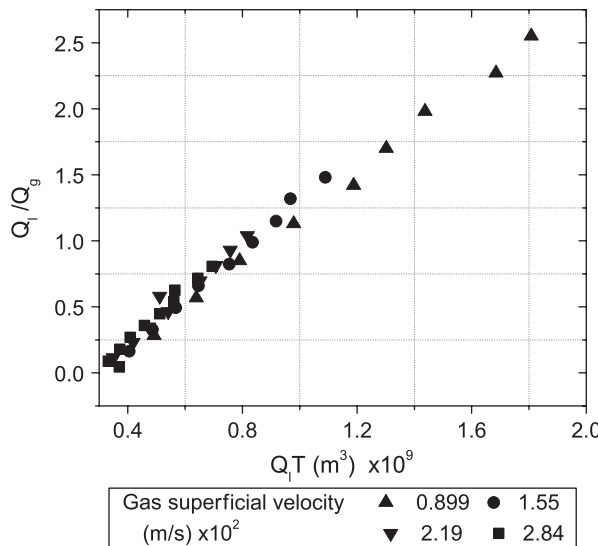


Fig. 14. Plot of Q_l/Q_g vs $Q_l T$, for 0.11 mm ID nozzle and air–water system.

clear that the resulting values of We_g are small, and the term associated with We_g in Eq. (6) may be neglected. In fact the difference in values \bar{V}_{\max} calculated with and without the We_g term was less than 6% for the whole range of We_g . This suggests that the gas phase can be treated as a quasi-static system. This result is interesting because it shows We_g and hence surface tension γ have limited influence on the Taylor bubble size formed by this mechanism. Of course, if γ is sufficiently small, the bubble might not remain attached to the nozzle long enough to become a Taylor bubble (Bhunia et al., 1998).

Nevertheless, the full set of Eqs. (7)–(9) is solved. To examine the values of the calculated parameters V_s and V_{\max} with those obtained from the experiment, the sum of expressions (1) and (2) can be rearranged as follows:

$$\frac{Q_l}{Q_g} = \frac{1}{\bar{V}_s} (Q_l T) - \frac{V_{\max} - V_i}{V_s}, \quad (14)$$

where

$$T = t_s + t_t. \quad (15)$$

The Taylor bubble volume can be calculated from Eq. (14) as follows:

$$\bar{V}_b = V_s + \left(\frac{Q_g}{Q_l} \right) [\bar{V}_{\max} - \bar{V}_i]. \quad (16)$$

Plotting the experimental data of air–water for nozzle size 0.11 mm and air–octane for nozzle size 0.34 mm in terms of Q_l/Q_g versus $Q_l T$ allows V_s and $(V_{\max}^{\exp} - V_i^{\exp})$ to be calculated (Figs. 14 and 15). These values are made dimensionless by dividing with d^3 and are tabulated in Tables 2 and 3. The fact that the points nearly collapse onto a single straight line shows V_s and V_{\max} to be nearly independent of the gas and liquid flow rates.

For the air–water results, it can be seen that \bar{V}_s^{\exp} increased with decreasing gas flow rate but nevertheless was close to the value of $\pi/6 = 0.524$ obtained if a sphere is assumed to

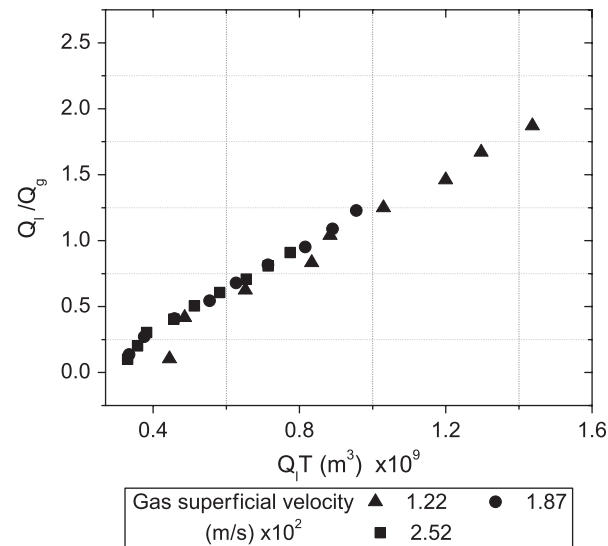


Fig. 15. Plot of Q_l/Q_g vs $Q_l T$, for 0.34 mm ID nozzle and air–octane system.

Table 2

Experimental and theoretical volumes for the air–water case and 0.11 mm ID nozzle

Gas flow rate	0.42 mL/min	0.73 mL/min	1.03 mL/min	1.34 mL/min
\bar{V}_s^{\exp}	0.592	0.515	0.511	0.476
$\bar{V}_{\max}^{\exp} - \bar{V}_i^{\exp}$	0.309	0.317	0.284	0.297
$\bar{V}_{\max} - \bar{V}_i$	0.170	0.156	0.159	0.165

Table 3

Experimental and theoretical volumes for the air–octane case and 0.34 mm ID nozzle

Gas flow rate	0.56 mL/min	0.89 mL/min	1.22 mL/min
\bar{V}_s^{\exp}	0.641	0.603	0.588
$\bar{V}_{\max}^{\exp} - \bar{V}_i^{\exp}$	0.239	0.225	0.232
$\bar{V}_{\max} - \bar{V}_i$	0.133	0.135	0.133

form initially (within 11%). Similarly, the volume of the liquid from the moment the bubble touches the wall until the Taylor bubble breaks ($\bar{V}_{\max} - \bar{V}_i$) also showed an increasing trend with decreasing gas flow rate. These values are however consistently under-predicted by the model (by about 51%).

Similar conclusions can be drawn from the results for the air–octane system with nozzle size 0.34 mm, shown in Fig. 15 and Table 3. The differences in this case between model and experiments are of the same order as in the air–water system (18% difference for \bar{V}_s and 44% in $\bar{V}_{\max} - \bar{V}_i$).

It can be concluded that there is some error in assuming the initial, pre-Taylor bubble to be a perfect sphere. In fact, larger experimental volumes, \bar{V}_s^{\exp} , imply that the bubbles were slightly elongated while the error was larger for the larger nozzle (Table 3). The deviation may be partly related to the non-concentric arrangement of the nozzle in the tube. From Eq. (16) it can also be deduced that experimental bubble sizes are

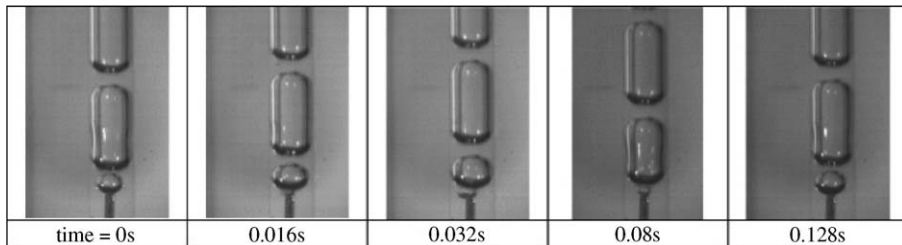


Fig. 16. Base pairing causing the formation of a Taylor bubble from a Taylor bubble in octane for 0.11 mm ID nozzle. Liquid superficial velocity, $U_{LS} = 0.0051$ m/s, gas superficial velocity, $U_{GS} = 0.019$ m/s.

larger than those predicted by the model proposed here. This may be due to stabilisation effects in the second stage of Taylor bubble formation associated with the neglected inertial and viscous forces or with the non-concentric arrangement of the nozzle in the tube.

Experimental values of $(\bar{V}_{\max}^{\exp} - \bar{V}_i^{\exp})$ show little variation ($< 6\%$ from average) with gas flow rates in both of Tables 2 and 3 consistent with the earlier discussion of We_g . A similar conclusion can be drawn from the relatively good correlation to a straight line of the points in Figs. 14 and 15 for each of the gas flow rates as to the limited effect of liquid flow rates on the values of $(\bar{V}_{\max}^{\exp} - \bar{V}_i^{\exp})$. The effect of changing the nozzle on the other hand from 0.11 to 0.34 mm reduced $(\bar{V}_{\max}^{\exp} - \bar{V}_i^{\exp})$ by around 40%. Formation times by mechanism 3 are therefore mostly functions of nozzle size and flow rates.

For the same flow rate ratios, comparing the two nozzles, with $\bar{V}_{\max}^{\exp} - \bar{V}_i^{\exp}$ taken as the average of the experimental results in Tables 2 and 3, shows the 0.11 mm ID nozzle to produce the larger bubbles.

$$\frac{V_b^{0.34 \text{ mm ID}}}{V_b^{0.11 \text{ mm ID}}} \approx \frac{\pi/6 + 0.232(Q_g/Q_l)}{\pi/6 + 0.302(Q_g/Q_l)} < 1 \quad \text{for } \frac{Q_g}{Q_l} > 0. \quad (17)$$

3.4. Bubble size modification

3.4.1. Bubble pairing

Bubble pairing is a common phenomenon at high flow rates (Clift et al., 1978), where a new bubble before it can break away from the nozzle coalesces with the bubble formed just before it which would quickly neck and detach (Fig. 16). Due to the slow movement of Taylor bubbles, the phenomenon appeared at much lower flow rates than would be observed in an unconfined liquid with non-Taylor bubbles. This would repeat for the next bubble forming at the nozzle until enough liquid had accumulated behind the large bubble such that no further pairing could take place.

An idealised schematic of pairing between a Taylor bubble and a forming bubble for coaxial inlets is given in Fig. 17. After the neck breaks up and the Taylor bubble forms, the volume of the neck is distributed between the formed bubble and the nozzle (depending on the location along the neck at which the breakage occurs). The volume left attached to the nozzle forms a small spherical bubble with diameter d_{B0} .

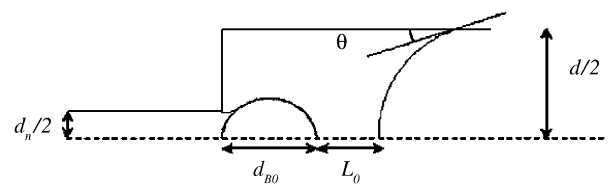


Fig. 17. Schematic of a formed Taylor bubble and the volume of gas formed by the collapse of the neck still attached to the nozzle.

Experimental observations (Fig. 16) show no gas volume to be left behind at the nozzle, ($d_{B0} \sim 0$). The profile of the back of the formed bubble is taken as spherical with a radius of curvature determined from the (apparent or actual) contact angle θ (Fig. 17).

With constant volumetric flow rates of gas, Q_g , and liquid, Q_l , the diameter d_B of the forming bubble with time t is given by

$$d_B = \sqrt[3]{\frac{6}{\pi} Q_g t + d_{B0}^3}. \quad (18)$$

The initial distance separating the formed bubble from the nozzle is determined as $d_{B0} + L_0$. The distance separating the formed bubble from the nozzle at time t is given by

$$L = (d_{B0} + L_0) + \frac{4(Q_g + Q_l)}{\pi d^2} t. \quad (19)$$

Pairing occurs when the diameter, d_B of the forming bubble, and the separation L become equal i.e.,

$$\frac{6}{\pi} Q_g t + d_{B0}^3 = \left((d_{B0} + L_0) + \frac{4(Q_g + Q_l)}{\pi d^2} t \right)^3. \quad (20)$$

In the above analysis the time needed for coalescence is neglected. With the surfactant free low viscosity fluids used in this study and flow rates investigated the time for the bubbles to be in touch is much larger than the time necessary for the film in between them to drain. Further, from the photograph sequences, no film between two coalescing bubbles could be seen in more than one frame, suggesting very fast coalescence times. For coalescence to occur the above equation must have real roots for t that also satisfy the condition

$$0 < t < \frac{\pi(d^3 - d_{B0}^3)}{6Q_g}. \quad (21)$$

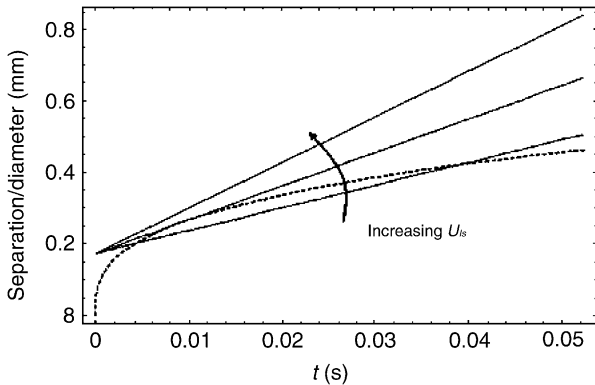


Fig. 18. The change of separation L (solid line) and forming bubble diameter d_B (dashed line) with time.

The upper limit in expression (21) is a physical limit, as the bubble diameter cannot exceed that of the tube. When it does reach that size, Eq. (18) is no longer valid.

As the existence of a valid solution for t from Eq. (20) is a necessary condition for pairing to occur it is worth investigating the properties of Eq. (20) which guarantee the existence of this solution. For flow rate combinations which form Taylor bubbles, and for a given gas flow rate, there is always a liquid flow rate at which pairing occurs. In Fig. 18, the LHS (solid) and the RHS (dashed) of Eq. (20) are plotted for various U_{ls} values. Clearly when these curves cross or touch, pairing occurs. Increasing the liquid flow (provided that Taylor bubbles still form), eventually causes pairing to stop (see Fig. 18). The condition for not having a solution t is $D > 0$, where D is the discriminant of the cubic equation (20). The stability boundary of the pairing mechanism is given by $D = 0$.

The quantities d_{B0} and L_0 need to be supplied and are usually difficult to predict. If the volume of liquid before the bubble breaks V_{\max} is known, then mass conservation necessitates that Eq. (22) is satisfied

$$V_{\max} = \underbrace{\frac{\pi d^2}{4} \left(L_0 + d_{B0} + \frac{d}{2} (\sec \theta - \tan \theta) \right)}_{\text{Volume of cylinder from nozzle to contact point}} - \underbrace{\frac{\pi d^3 (2 + \sin \theta) (1 - \sin \theta)^2}{24 \cos^3 \theta}}_{\text{Volume of bubble cap}} - \underbrace{\frac{\pi d_{B0}^3}{6}}_{\text{Initial sphere volume}}. \quad (22)$$

If d_{B0} is set to zero, and the V_{\max} from the model developed for bubble formation in Section 3.2 is used, L_0 can then be predicted from Eq. (23):

$$L_0 = \frac{4}{\pi d^2} \left(V_{\max} + \frac{\pi d^3 (2 + \sin \theta) (1 - \sin \theta)^2}{24 \cos^3 \theta} \right) - \frac{d}{2} (\sec \theta - \tan \theta). \quad (23)$$

The value of θ (real or apparent) depends on the capillary number Ca (Chebbi, 2003). For $d_{B0} = 0$, expression $D = 0$ gives

$$Q_l = \frac{1 - \frac{9}{2}(L_0^2/d^2)}{\frac{9}{2}(L_0^2/d^2)} Q_g. \quad (24)$$

This equation can be used to obtain boundaries between pairing and non-pairing Taylor flow (Section 3.5).

3.4.2. Bubble coalescence

Depending on the flow conditions, small non-Taylor bubbles can be formed, which may pair near the inlet to Taylor (as seen previously) or non-Taylor bubbles (smaller than tube diameter). The non-Taylor bubbles can undergo further modification away from the inlet by coalescing with other bubbles. Coalescence of bubbles within the channel was nearly always seen for the small nozzle and high liquid flow rates which resulted in small non-Taylor bubbles that did not pair. In such a sequence most bubbles had very similar velocities. Occasionally a bubble formed which had a higher rise speed than the preceding one. At a point along the channel, these two bubbles coalesced to form a Taylor bubble (Fig. 19). A Taylor bubble is much slower than the non-Taylor bubbles so that subsequent non-Taylor bubbles caught-up and coalesced with the Taylor bubble causing it to grow further. The process continued until another pair of non-Taylor bubbles coalesced upstream of the Taylor bubble. All remaining non-Taylor bubbles in between subsequently coalesced with the Taylor bubble downstream (if the channel length was sufficient). The final distribution of Taylor bubble sizes was observed to be determined by the frequency of coalescence of two non-Taylor bubbles.

Distributions of sizes for these cases were not investigated in the current work because the channel length was not always sufficient for all the non-Taylor bubbles to coalesce. However, from qualitative observations it can be concluded that the range of final Taylor bubble sizes increased with increasing flow rates. It would be wise to avoid the conditions that favour this mechanisms if regular Taylor bubbles are required.

Bubble coalescence was most probably caused by the dependence of bubble velocity on bubble size. It appears that even small variations in size affect the velocity with the smaller bubbles having higher velocities than larger bubbles. Smaller bubbles occupy regions in the tube with higher average velocities. The reason why a slightly different bubble is randomly formed could be due to minor flow or pressure fluctuations.

3.5. Maps of Taylor bubble formation/modification by pairing or coalescence

The gas and liquid superficial velocities for which the different Taylor bubble formation mechanisms appeared can be seen in Fig. 20 for the air-octane system and the large size nozzle (ID 0.34 mm). In the majority of cases Taylor bubbles formed at the nozzle without any further modification downstream. However, for low U_{ls} , pairing at the inlet occurred. Eqs. (23)–(24) can be used to find the limiting conditions for bubble pairing

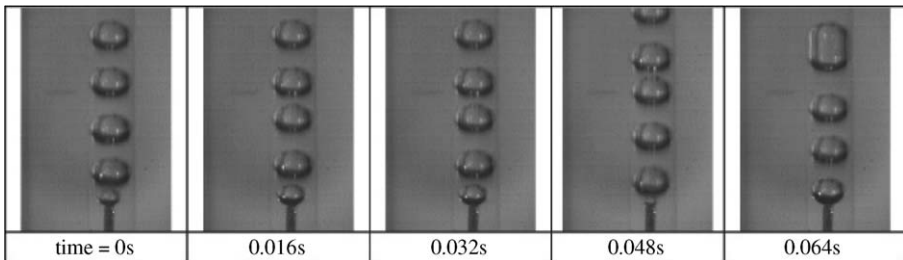


Fig. 19. Non-Taylor bubble coalescence causing the formation of a Taylor bubble in octane for a 0.11 mm ID nozzle. Liquid superficial velocity, $U_{LS} = 0.0204 \text{ m/s}$, gas superficial velocity, $U_{GS} = 0.019 \text{ m/s}$.

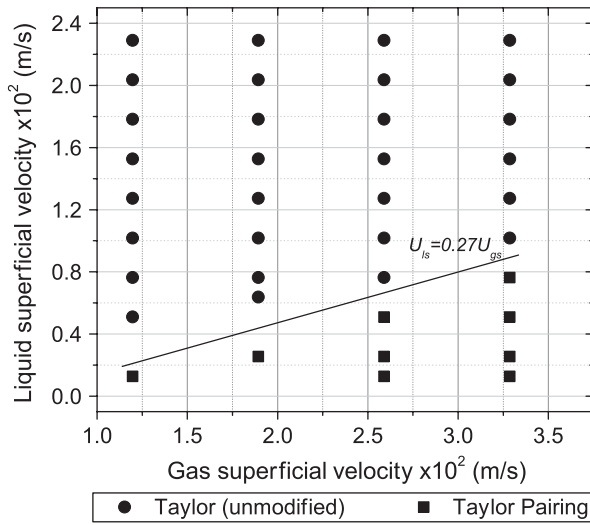


Fig. 20. Map of post formation bubble volume modification in octane for a 0.34 mm ID nozzle.

to occur. L_0 was calculated from Eq. (23) (with $\theta \approx \frac{\pi}{4}$ as was estimated from the photos). Eq. (24) then becomes

$$U_{ls} = 7.30 U_{gs}. \quad (25)$$

According to the above equation bubble pairing should occur for the entire range of flow rates studied, which clearly was not the case (compare Eq. (25) with the experimental slope in Fig. 20). It is interesting to note though that the boundary in Fig. 20 is a straight line passing through the origin, similar to Eq. (25). Studying the experimental results carefully revealed that:

- (1) On bubble detachment from the nozzle, the gas meniscus disappeared into the nozzle. A length of time passed before the interface emerged again which caused L_0 to be larger than would be predicted by Eq. (23).
- (2) The non-concentric arrangement of the nozzle increased the initial length L_0 which the forming bubble diameter needed to match before the pairing occurred.

Eq. (24) can be modified to account for nozzle eccentricity from the tube axis and can still be used if an expression for L_0 can be found which accounts for liquid entering the nozzle. In its current form it may be useful as a ‘worst case’ analysis method.

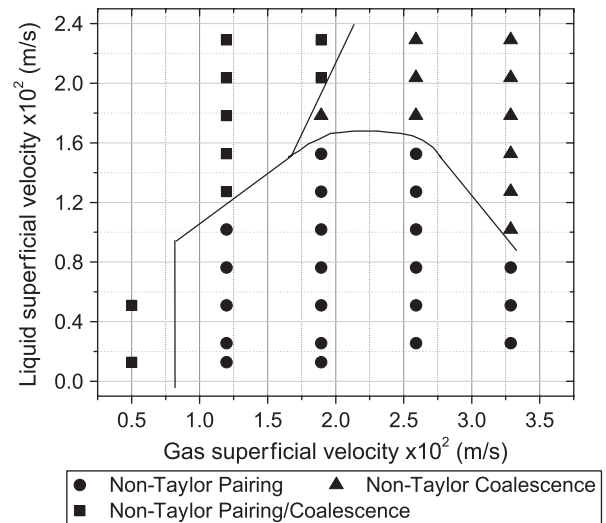


Fig. 21. Map of post formation bubble volume modification in octane for a 0.11 mm ID nozzle.

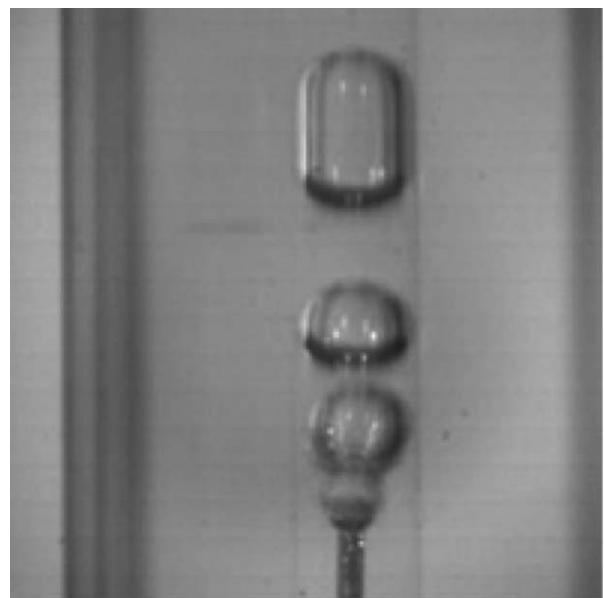


Fig. 22. Non-Taylor bubble pairing followed by coalescence causing the formation of a Taylor bubble in octane for a 0.11 mm ID nozzle. Liquid superficial velocity, $U_{LS} = 0.0204 \text{ m/s}$, gas superficial velocity, $U_{GS} = 0.0259 \text{ m/s}$.

A similar map of Taylor bubble formation mechanisms is shown in Fig. 21 for air–octane with the small gas nozzle (ID 0.11 mm). In the majority of cases all initial bubbles are non-Taylor and become Taylor either by pairing or coalescence or even a combination of the two cases (see Fig. 22 for an example of combined pairing and coalescence).

Maps for air–water system are not presented because for the larger nozzle the mechanism of formation alternated between mechanism 1 and mechanism 2 for the same gas and liquid flow rates while for the small nozzle, Taylor bubbles were always formed by mechanism 3 without further modification.

4. Conclusions

Taylor bubble formation in capillary tubes has been studied theoretically and experimentally in a co-flow gas–liquid contacting arrangement for two liquids with different properties. The following can be concluded:

- (1) Three different mechanisms of bubble formation were observed. With careful design of the capillary outlet, uniform bubble sizes were produced in the majority of cases.
- (2) Mechanism 3 in which the bubble necked and broke, led to the formation of Taylor or non-Taylor bubbles and was found to be prevalent for most conditions studied.
- (3) Taylor bubbles formed with mechanism 3 were found to have periods that depend mainly on gas and liquid flow rates and nozzle size and were almost independent of the surface tension. A concentric inlet arrangement can therefore be used to generate bubbles of a specific volume irrespective of the liquid used.
- (4) The simple model proposed for Taylor bubble lengths formed by mechanism 3 was found to agree with the experimental trends satisfactorily apart from low liquid and gas flow rates where pressure fluctuations caused by long bubbles exiting the tube influence bubble formation at the inlet. The model can be further improved by taking into account the shape of the bubble at the nozzle before it reaches the capillary wall and by including viscous and inertial phenomena as well as further investigating the nature of the contact with the wall.
- (5) Bubble pairing and coalescence were present in some cases and considerably modified the sizes of the already formed bubbles. For cases where coalescence was present away from the nozzle, a wide distribution of bubble sizes was obtained.
- (6) A simple bubble pairing model was proposed for predicting pairing for concentric tube/nozzle arrangements. The model over-predicted the range of liquid flow rates at which pairing was observed experimentally. The model can be modified by taking into account any deviations from the concentric inlet arrangement inherent in the setup as well as the exact initial position of the meniscus after the bubble neck breakage. The model in its current form may however be used as a ‘worst case’ predictor of bubble pairing.

Notation

Ca	capillary number $\mu U_b / \gamma$
d	tube diameter, m
d_b	bubble diameter, m
d_{B0}	diameter of spherical bubble remaining at nozzle after breakup, m
d_n	internal nozzle diameter, m
D	determinant of cubic Eq. (20)
Eo	Eötvos number $g \Delta \rho d^2 / \gamma$
g	acceleration due to gravity, m/s ²
l	axial length from the wall contact point to nozzle, m
L	length of liquid separating formed and forming bubbles, m
L_0	length of liquid separating formed and forming bubbles at breakup, m
p	pressure, N/m ²
Δp	pressure drop across the bubble interface, N/m ²
Q	volumetric flow rate, m ³ /s
r	radial coordinate, m
Re	liquid Reynolds number $\rho U_l d / \mu$
S	arc length, m
t_s	time for a spherical bubble to form and touch the tube walls, s
t_t	time for a Taylor bubble between reaching the tube wall and detaching from the nozzle, s
T	total time for bubble formation, s
u	average cross sectional velocity, m/s
U	superficial velocity, m/s
V_s	volume of spherical bubble touching the tube walls, m ³ /s
V_i	volume of liquid behind spherical bubble when it first touches the walls, m ³ /s
V_{\max}	maximum volume of liquid behind a Taylor bubble before it breaks, m ³ /s
We_g	gas Weber number $\rho_g u_{g0}^2 d / \gamma$
We_l	liquid Weber number $Re Ca$
z	axial coordinate, m

Greek letters

α	angle that the tangent to the interface forms with a horizontal line, °
γ	interfacial tension, N/m
θ	apparent or real contact angle of a formed bubble with tube wall, °
θ_1	apparent or real contact angle of a forming bubble with tube wall, °
θ_2	real contact angle of a forming bubble with the nozzle, °
λ	arc length from wall contact point to nozzle, m
μ	viscosity, kg/ms
ρ	density, kg/m ³
$\Delta\rho$	density difference between the dense and light phases, kg/m ³

Subscripts

<i>b</i>	bubble
<i>g</i>	gas phase
<i>gs</i>	gas superficial
<i>g0</i>	gas inlet values
<i>l</i>	liquid phase
<i>ls</i>	liquid superficial

Acknowledgements

This work was supported by the EU KEMiCC project G1RD-CT2000-00469. The authors would also like to thank the EPSRC Instrument Pool for providing the high speed camera.

References

- Aussillous, P., Quéré, D., 2000. Quick deposition of a fluid on the wall of a tube. *Physics of Fluids* 12, 2367–2371.
- Berćic, G., Pintar, A., 1997. The role of gas bubbles and liquid slug lengths on mass transport in the Taylor flow through capillaries. *Chemical Engineering Science* 52, 3709–3719.
- Bhunia, A., Pais, S.C., Kamotani, Y., Kim, I.H., 1998. Bubble formation in a coflow configuration in normal and reduced gravity. *A.I.Ch.E. Journal* 44, 1499–1509.
- Bretherton, F.P., 1961. The motion of long bubbles in tubes. *Journal of Fluid Mechanics* 10, 166–188.
- Chebbi, R., 2003. Deformation of advancing gas–liquid interfaces in capillary tubes. *Journal of Colloid and Interface Science* 265, 166–173.
- Chen, J.D., 1986. Measuring the film thickness surrounding a bubble inside a capillary. *Journal of Colloid and Interface Science* 109, 341–349.
- Clift, R., Grace, J.R., Weber, M.E., 1978. *Bubbles, Drops and Particles*. Academic Press, New York.
- Edvinsson, R.K., Irandoost, S., 1996. Finite-element analysis of Taylor flow. *A.I.Ch.E. Journal* 42, 1815–1823.
- Giavedoni, M.D., Saita, F.A., 1997. The axisymmetrical and plane cases of gas phase steadily displacing a Newtonian liquid—A simultaneous solution of the governing equations. *Physics of Fluids* 9, 2420–2428.
- Giavedoni, M.D., Saita, F.A., 1999. The rear meniscus of a long bubble steadily displacing a Newtonian liquid in a capillary tube. *Physics of Fluids* 11, 786–794.
- Hernandez-Baltazar, E., Gracia-Fadrique, J., 2005. Elliptic solution to the Young-Laplace differential equation. *Journal of Colloid and Interface Science* 287, 213–216.
- Irandoost, S., Andersson, B., 1988. Mass-transfer and liquid-phase reactions in a segmented 2-phase flow monolithic catalyst reactor. *Chemical Engineering Science* 43, 1983–1988.
- Kim, I.H., Kamotani, Y., Ostrach, S., 1994. Modelling bubble and drop formation in flowing liquids in microgravity. *A.I.Ch.E. Journal* 40, 19–28.
- Kreutzer, M.T., Kapteijn, F., Moulijn, J.A., Kleijn, C.R., Heiszwolf, J.J., 2005. Inertial and interfacial effects on the pressure drop of Taylor flow in capillaries. *A.I.Ch.E. Journal* 50(9), 2428–2440.
- Kumar, R., Kuloor, N.R., 1970. The formation of bubbles and drops. *Advances in Chemical Engineering* 8, 256–365.
- Nahra, H.K., Kamotani, Y., 2003. Prediction of bubble diameter at detachment from a wall orifice in liquid cross-flow under reduced and normal gravity conditions. *Chemical Engineering Science* 58, 55–69.
- Oğuz, H.N., Zeng, J., 1998. In: *Proceedings of the Fourth Microgravity Fluids Physics and Transport Phenomena Conference*, August, Cleveland, Ohio.
- Pamperin, O., Rath, H., 1995. Influence of buoyancy on bubble formation at submerged orifices. *Chemical Engineering Science* 50, 3009–3024.
- Salman, W., Gavriilidis, A., Angelis, P., 2004. A model for predicting axial mixing during gas–liquid Taylor flow in microchannels at low Bond number. *Chemical Engineering Journal* 101, 391–396.
- Serizawa, A., Feng, Z., Kawara, Z., 2002. Gas–liquid two-phase flow in microchannels Part I: Two-phase flow patterns. *Experimental Thermal and Fluid Sciences* 26, 703–714.
- Taylor, G.I., 1960. The rear meniscus of a long bubble steadily displacing a Newtonian liquid in a capillary tube. *Journal of Fluid Mechanics* 10, 161–165.
- Thulasidas, T.C., Abraham, M.A., Cerro, R.L., 1995. Bubble-train flow in capillaries of circular and square cross section. *Chemical Engineering Science* 50, 183–199.
- Thulasidas, T.C., Abraham, M.A., Cerro, R.L., 1997. Flow patterns in liquid slugs during bubble-train flow inside capillaries. *Chemical Engineering Science* 52, 2947–2962.
- Thulasidas, T.C., Abraham, M.A., Cerro, R.L., 1999. Dispersion during bubble-train flow in capillaries. *Chemical Engineering Science* 54, 61–76.
- Triplett, K.A., Ghiaasiaan, S.M., Abdel-Khalik, S.I., Sadowski, D.L., 1999. Gas–liquid two-phase flow in microchannels Part I: two-phase flow patterns. *International Journal of Multiphase Flow* 25, 377–394.